Chemical imaging of oxide confinement layers in GaAs/AlxGa1–xAs VCSELs

Merwan Mokhtari, Philippe Pagnod-Rossiaux, Christophe Levallois, Alexandre Pofelski, François Laruelle, Gianluigi A Botton, Jean-Pierre Landesman

Chemical imaging of oxide confinement layers in $GaAs/Al_xGa_{1-x}As$ VCSELs

Merwan Mokhtari[1]‡, **Philippe Pagnod-Rossiaux**[2], **Christophe Levallois**[3], **Alexandre Pofelski**[4], **François Laruelle**[2], **Gianluigi A. Botton**[4] and **Jean-Pierre Landesman**[3]

[1] Univ Rennes, CNRS, IPR – UMR 6251, F-35000 Rennes, France
[2] 3SP Technologies SAS, 91625 Nozay, France
[3] Univ Rennes, INSA Rennes, CNRS, Institut FOTON – UMR 6082, F-35000 Rennes, France
[4] Department of Materials Science and Engineering, McMaster University, Hamilton, ON, Canada, Canada

E-mail: mmokhtari@3spgroup.com

9 May 2022

Abstract. The authors have studied the lateral oxidation of $Al_xGa_{1-x}As$ layers buried in vertical-cavity surface-emitting lasers using cross-sectional scanning transmission electron microscopy coupled with electron energy loss spectroscopy. Chemical maps and composition profiles of the oxidized AlOx layers have been produced. The sensitivity is such that trace compositions of a few % *As* and *Ga* can be detected in the AlOx with a spatial resolution of few nanometers on the recorded chemical maps. To demonstrate the performance of the mapping technique, we compare results from an area in the VCSEL which is pure $Al_xGa_{1-x}As$ to an oxidized area. These measurements are performed on a thin sample prepared by the focused ion beam technique within an actual VCSEL, which makes the mapping technique applicable for degradation investigations in devices at different stages of their lifetime. More generally, this measurement method is effective for detailed evaluation of AlOx layers and their fabrication process.

1. Introduction

Aluminium oxide layers (commonly called AlOx layers) are used to confine charge carriers and photons within the emission area of $Al_xGa_{1-x}As$ vertical-cavity surface-emitting lasers (VCSELs). These AlOx layers are produced by lateral oxidation at elevated temperature (typically around 380 to 460 °C), under humid ambient, of $Al_xGa_{1-x}As$ with high *Al* content [1]. The lateral oxidation process involves complex redox reactions for the different elements *As*, *Ga* and *Al* as well as transport mechanisms for the gas phase reaction products through the porosity of the AlOx layer formed and / or at the interfaces between this AlOx layer and the neighbouring un-oxidized layers [2]. This fabrication process raises a number of questions related to the VCSEL reliability [3]. Firstly, the oxide formation introduces tensile strain in

‡ Present address: 3SP Technologies SAS, 91625 Nozay, France

the adjacent layers due to shrinkage of the AlOx compared to $Al_xGa_{1-x}As$ [4]. Secondly, the chemical stability of the oxide phases present in the AlOx layer may also be an issue [5]. Finally, voids at the interfaces of the AlOx layer have been observed when volatile products (AsH_3 or elemental As) are formed in excess of some limit [6]. It is therefore crucial to monitor the chemical composition within the AlOx layer and close to its interfaces, and to determine composition profiles for the different elements. Our goal is to analyze the composition in AlOx layers with the highest possible spatial resolution. This challenge has been discussed in a limited number of articles. Targeted defect analysis in VCSEL oxide windows has been reported employing a focused ion beam scanning electron microscope (FIB-SEM) to sputter and image successive cross sections (slice and view technique) in order to produce a 3D reconstruction of the oxide aperture region [7]. Transmission electron microscopy (TEM) energy dispersive X-ray spectroscopy performed on cross-sectional samples can be considered [8, 9] with limited spatial resolution.

2. Experimental

For the present study, VCSEL devices designed to operate at a wavelength of 850 *nm* were used. The material was grown by metalorganic vapor phase epitaxy on (100) GaAs substrates. Si and C dopants were used for the n- and p-parts of the overall structure. The Bragg mirrors consist in $Al_{0.12}Ga_{0.88}As/Al_{0.9}Ga_{0.1}As$ pairs (30 and 16 pairs for the n-doped bottom and the p-doped top mirror, respectively). The active area includes five $In_{0.08}Ga_{0.92}As/Al_{0.4}Ga_{0.6}As$ quantum wells (QWs). Above the active area two $Al_{0.98}Ga_{0.02}As$ layers (thickness 30 *nm*), devoted to the lateral oxidation, were grown. Following epitaxial growth, reactive ion etching in a $SiCl_4/He$ inductively coupled plasma is applied to form circular shaped mesas. These mesas were subsequently oxidized to define the AlOx layers. Oxidation was carried at temperatures between 420 and 450 °C, in a humid atmosphere made of a N_2H_2/H_2O gas flow. The $Al_{0.98}Ga_{0.02}As$ layers oxidation length depends mainly on the temperature, H_2O flow rate and pressure and oxidation time. An AlOx lateral extension of 9 μm was aimed and controlled in-situ during oxidation by optical reflectivity monitoring [10]. For some of the samples, in-situ annealing was also performed immediately after oxidation. Figure 1 shows the overall structure where electrical n- and p- contacts have been added for clarity. An enlarged cross-section view of the oxidized area is also presented.

We prepared our TEM samples through the VCSEL structures using the focused ion beam (FIB) technique. The VCSEL samples were introduced in a Zeiss NVision 40 dual beam scanning electron microscope which allowed us to prepare very thin slabs (thickness typically 80 *nm*) precisely located in the region of interest. The thin slabs were then transferred into a high-resolution FEI Titan Cubed 80–300 microscope equipped with Corrected Electron Optical Systems (CEOS) on both the probe and image forming lens systems. For the present work, a beam energy of 200 keV was selected to find a compromise between spatial resolution and radiation damages. The microscope was operated in high-resolution scanning transmission electron microscopy (STEM) mode with a convergence angle of 19.8 mrad and a probe current between 50 and 100 pA. The electron energy loss spectroscopy (EELS)

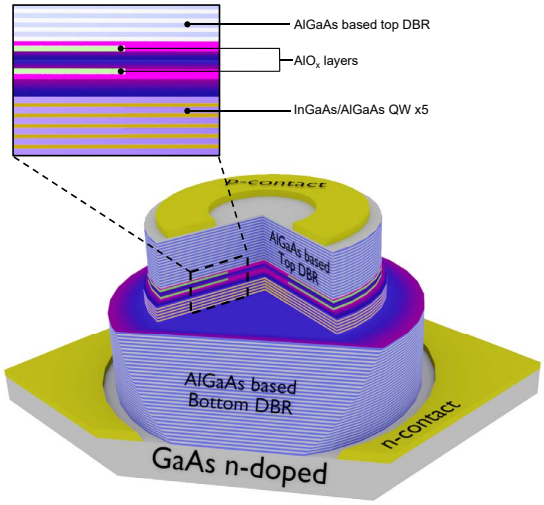

Figure 1. VCSEL structure, showing the epitaxial layer sequence and the n- and p- metal contacts. The inset shows the structure details in the area of the $In_{0.08}Ga_{0.92}As/Al_{0.4}Ga_{0.6}As$ QWs and $Al_{0.98}Ga_{0.02}As$ layers for lateral oxidation.

experiments were realized with a Gatan GIF Quantum spectrometer using a collection angle of 56.8 mrad, a dispersion of 0.5 eV/channel and the K2 IS Summit direct electron detection camera. Figure 2 shows raw EELS data recorded in a pristine $Al_xGa_{1-x}As$ and in an oxidized area.

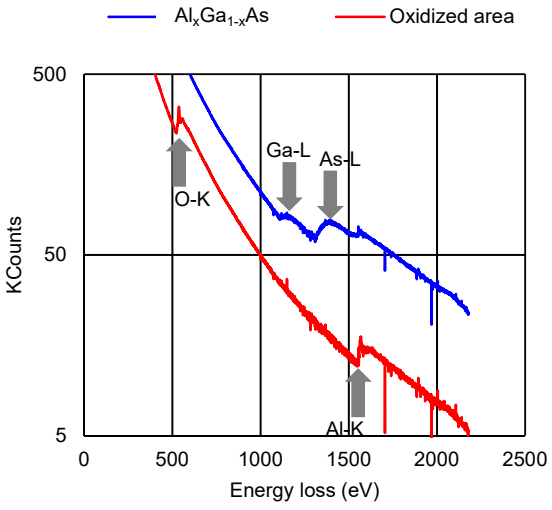

Figure 2. Electron energy loss spectra measured in a pristine $Al_xGa_{1-x}As$ area (blue curve) and in an oxide area (red curve). The energy positions for the $O-K$, $Al-K$, $Ga-L_{2,3}$ and $As-L_{2,3}$ edges are indicated by the vertical arrows.

The EELS edges for the different elements can be observed. Quantification of these elements was performed using the EELS module of the Gatan Microscopy Suite 3 software. This module takes into account the overlap between signals for atoms with neighbouring

edges [11, 12]. As can be seen in fig. 2, the $Ga-L$ and $As-L$ edges for example display such an overlap. An exponential background due to the lower energy losses (including plasmons and incident energy loss distribution) is subtracted [13]. The Hartree-Slater cross sections [14] were taken into account for this quantification. Note that no correction for the slab thickness was performed when processing the data. Finally, the quantification process computes the integrated intensity of each EELS curve, corresponding to each element in the sample, for energies above its threshold.

3. Results and Discussion

To map the chemical composition in different areas of the FIB samples, STEM hyperspectral images were recorded and further processed using the quantification module described. Figure 3 illustrates this combined high-resolution STEM imaging and chemical imaging procedure.

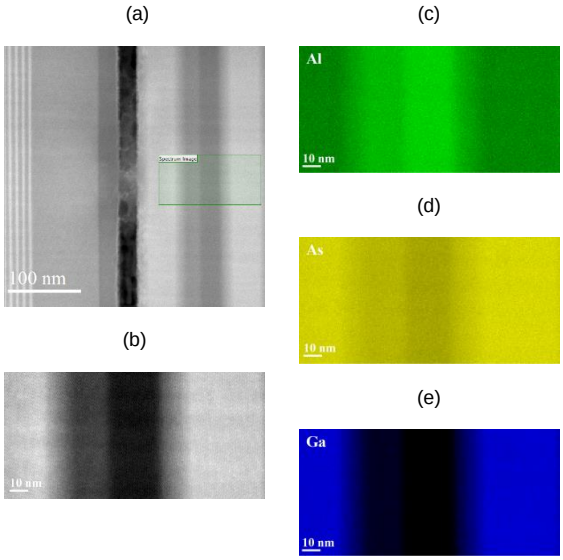

Figure 3. Scanning transmission electron microscopy images and energy loss integrated intensity maps for *Ga*, *Al* and *As* edges measured in an un-oxidized $Al_xGa_{1-x}As$ layer. (a): STEM image with the green rectangle representing the area mapped ; (b): High-resolution STEM image focused on the green rectangle labelled in (a); (c): EELS integrated intensity map for the *Al* element; (d): EELS integrated intensity map for the *As* element; (e): EELS integrated intensity map for the *Ga* element. Bright areas in (c), (d) and (e) indicate high concentrations of the respective chemical species. The layer appearing dark in (a) is the underlying oxide.

The *Al* and *Ga* maps show variations in intensity which are correlated with the atomic densities (related to the relative compositions) in the different layers. The *As* map also displays some intensity variation. However, the *As* atomic density is constant throughout the different layers mapped in the example of fig. 3 (no element V alloy in the samples). The reason for the modulation of the *As* EELS intensity is an artefact due to overlapping of the signal for atoms with neighbouring edges, typically *Ga*, which cannot be totally resolved by the data processing module. The magnitude of this artefact is discussed below. Note the dark layer in

fig. 3-a, corresponding to an almost fully oxidized $Al_{0.98}Ga_{0.02}As$ layer. The chemical images in fig. 3-c, 3-d and 3-e were taken on the neighbouring $Al_{0.98}Ga_{0.02}As$ layer, not fully oxidized for this particular sample (cf. sample structure in fig. 1).

From the maps shown in fig. 3, composition profiles across the different layers in the region of interest were reconstructed by averaging the chemical maps along the vertical direction. The results are shown in figure 4. One can observe that the line profiles reproduce accurately the composition changes for *Al* and *Ga*. The nominal compositions for these elements have been indicated in fig. 4. Each vertical line displays a change in composition. To precisely position these lines at the level of the points of change in slope, we focus on the *Ga* profile which shows the steepest variations compared to the *Al* profile. Starting from the outer layers with 12 % *Al* / 88 % *Ga*, the layers with graded composition (12 to 80 % *Al* / 88 to 20 % *Ga*, thickness 20 *nm*), are clearly visualized. The abrupt changes on each side of the $Al_{0.98}Ga_{0.02}As$ layer extend over less than 5 *nm*, which is thus an upper limit of the spatial resolution. The *Ga* signal appears proportional to the nominal *Ga* composition. The signal for *Al* varies linearly with the nominal *Al* composition, but with an offset. Since the *Al* is the atom with the highest energy edge, it is the one that is most sensitive to the effect of this offset. In addition, the *As* signal shows some modulation (about 21 % in magnitude) whereas this signal should be constant as the *As* composition is constant. These observations point to a processing artefact due to overlapping of the signal for atoms with neighbouring edges, *Ga* and *Al*. It is therefore even more sensitive to signal overlapping effects, especially when there are strong variations in the composition of *Ga* (resp. *Al*). The *Ga* is not (or less) affected by this problem as this element has the lowest EELS edge.

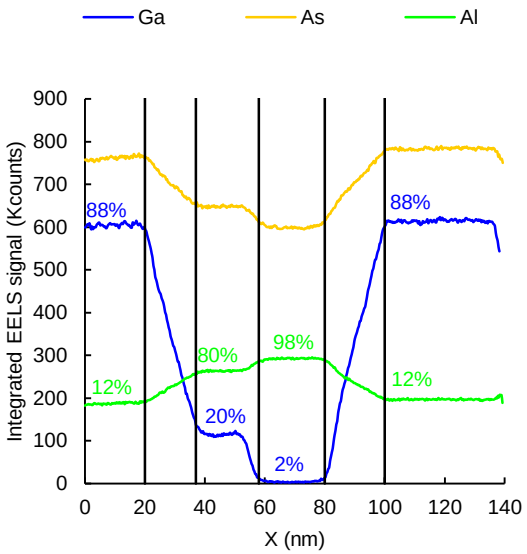

Figure 4. Line profiles from the integrated EELS intensity maps displayed in fig. 3 across the un-oxidized $Al_xGa_{1-x}As$ sequence for each element. The nominal relative *Ga* and *Al* compositions are indicated for each layer on the corresponding profiles. The vertical lines indicate interfaces between layers of different compositions or layers with gradual composition.

Next we measured similar images in a region including the AlOx layers. The results are shown in figure 5, for a sample oxidized 25 min. at 420 ° C. The N_2H_2/H_2O gas flow rates used yield an oxidation length of 11.5 μm for this sample. A slight difference (approximately 250 *nm*) can be observed in fig. 5-a for the oxidation length of the 2 AlOx layers. This difference could be due to a slight difference in the *Al* compositions.

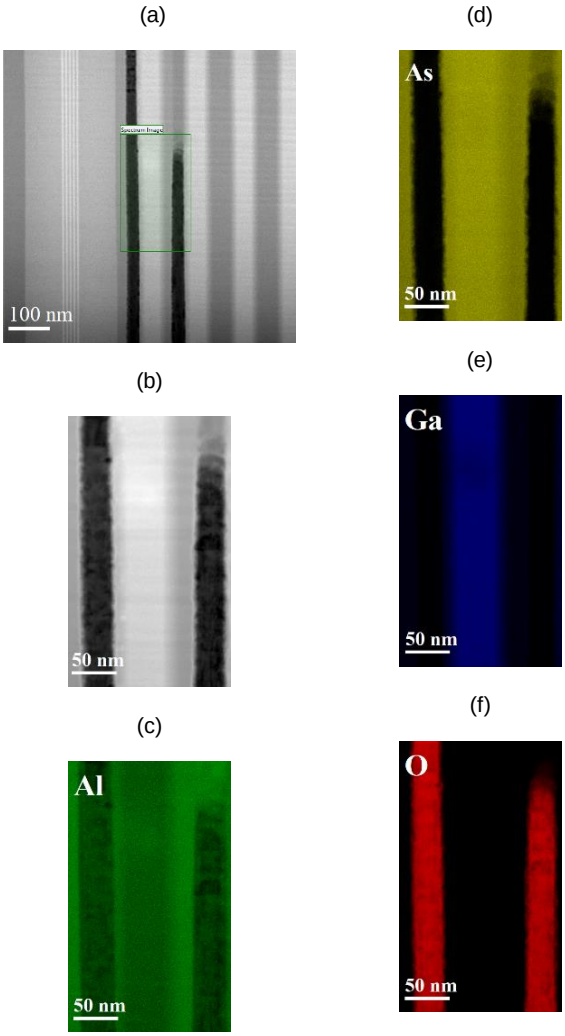

Figure 5. STEM images and EELS integrated intensity maps images for the Ga, Al, As and O chemical species measured in an area with oxidized layers. (a): STEM image with the green rectangle representing the area mapped ; (b): High-resolution STEM image focused on the green rectangle labelled in (a); (c): EELS integrated intensity map for the *Al* element; (d): EELS integrated intensity map for the *As* element; (e): EELs integrated intensity map for the *Ga* element ; (f): EELS integrated intensity map for the *O* element. Bright areas in (c), (d), (e) and (e) indicate high concentrations of the respective chemical species.

The intensity profiles derived from the measurements in figure 5 are shown in figure 6. The maps and profiles for *O* have been included. The shaded areas in fig. 6 highlight the oxide layers. They have been positioned according to the *O* intensity profile. The signal for *As* and *Ga* in these AlOx layers is very low but detectable: around 12.5 Kcounts for

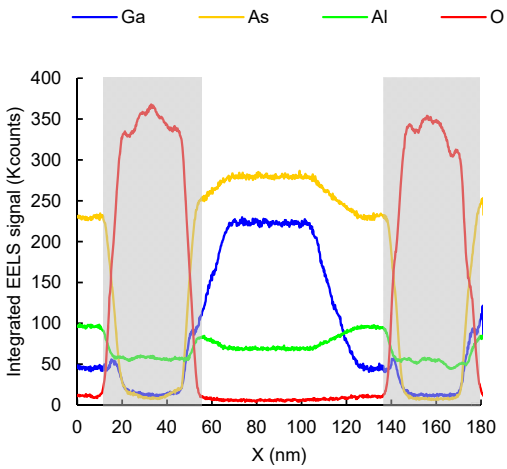

Figure 6. Line profiles from the EELS integrated intensity maps displayed in fig. 5 across the oxidized $Al_xGa_{1-x}As$ sequence for each element. Shaded rectangles mark the oxide layers.

Ga, corresponding to a composition of ~ 2.5 %. For *As* we estimate the composition in the AlOx layers to ~ 1.4 % of the *As* composition in a nominal un-oxidized layer. The *Al* profile indicates an apparent lower intensity in the AlOx layers than in the neighbouring $Al_xGa_{1-x}As$. However, we noted a strong change in the shape of the EELS curves immediately above the $Al-K$ edge upon oxidation. Changes in the chemical bonding of *Al* atoms can deeply affect the shape of the EELS signal in the area above the edge [15]. Since this effect was not taken into account in our data processing procedure, the signal for the *Al* profile is underestimated in the AlOx layers. The *O* signal detectable in the central (unoxidized) area originates from thin oxide layers formed at the two surfaces of the thin (80 *nm*) sample as it is exposed to air after the FIB thinning process.

The *O* profile can be used to evaluate the thickness of the AlOx layers: a thickness of 43 *nm* is found for both layers, which is higher than the nominal 30 *nm* of the initial $Al_{0.98}Ga_{0.02}As$ layers. Therefore, part of the adjacent $Al_{0.8}Ga_{0.2}As$ layers have also been oxidized. The small peaks on the *Ga* profile on the left edge of each AlOx layer seem to indicate that this increased thickness corresponds to some *Ga* oxide formed at the interface. As for the *As* profile, a gradual decrease of the intensity towards the center of the AlOx layer is clearly observed at both interfaces, indicating some migration towards these interfaces of elemental *As* resulting from the AlOx formation.

4. Conclusion

These preliminary results show that the coupling of EELS with high-resolution STEM imaging provides a means for efficient chemical mapping of nanometer layers such as the AlOx confinement layers of *GaAs* VCSELs. Taking benefit of the FIB preparation for the samples, we stress the fact that the mapping can be performed on real devices, opening the possibility for enhanced investigations of degradation mechanisms, and therefore more

performing reliability strategies. More generally, this measurement method is effective for detailed evaluation of AlOx layers and their fabrication process. For example, it can be used to study the AlOx layers used as gate oxide for *InZnO* thin-film transistors in order to enhance the performances [16]. The sensitivity of the technique, as well as the spatial resolution, still have to be quantified with care. However, initial promising figures for these have been given. More work is also necessary for a proper quantification procedure which will adequately remove the background, cover the overlap problem for the elements with neighbouring EELS edges and include the change of the EELS signals in the region close to the edge threshold upon oxidation. A correction for the thickness of the samples should also be included, based on the information from the zero-loss peak. The fact that the samples include layers whose composition is known with high accuracy (the $Al_{1-x}Ga_xAs$ layers which do not undergo oxidation) is very helpful in this first approach to estimate the composition in different areas of the AlOx layers, as was shown. The chemical mapping technique proposed allows in particular for an accurate determination of the AlOx layers thicknesses: the thickness is observed to increase during the lateral oxidation process but taking into account the details of the *Ga* profile, we suggest that part of the adjacent $Al_{0.8}Ga_{0.2}As$ layers have also been oxidized.

In this first evaluation, we have concentrated on measuring composition profiles far from the oxidation front of the AlOx layers, but of course another direction which we will investigate is the determination of the chemical composition of the phases formed at the oxidation front. This should produce a better insight into the mechanisms at play during this lateral oxidation process.

Acknowledgments

This work was partly supported by RENATECH (the French national network of facilities for micronanotechnology) and in particular LAAS-CNRS for oxidation processes. The sample preparation with FIB, as well as the STEM-EELS work was carried out at the Canadian centre for Electron Microscopy (CCEM), a national facility supported by the Canada Foundation for Innovation under the Major Science Initiative program (MSI), NSERC and McMaster University.

Data Availability Statement

The data that support the findings of this study are available from the corresponding author upon reasonable request.

The data that support the findings of this study are available from the corresponding author upon reasonable request.

References

[1] Huffaker D L, Deppe D G, Kumar K and Rogers T J 1994 *Appl. Phys. Lett.* **65** 97–99

[2] Langenfelder T, Schröder S and Grothe H 1997 *J. Appl. Phys.* **82** 3548–3551
[3] Hawkins B, Hawthorne R, Guenter J, Tatum J and Biard J 2002 Reliability of various size oxide aperture VCSELs *52nd Electronic Components and Technology Conference 2002.* (San Diego, CA, USA: IEEE) pp 540–550
[4] Mokhtari M, Pagnod-Rossiaux P, Levallois C, Laruelle F, Cassidy D T, Bettiati M and Landesman J P 2021 *Appl. Phys. Lett.* **118** 091102
[5] Guha S, Agahi F, Pezeshki B, Kash J A, Kisker D W and Bojarczuk N A 1996 *Appl. Phys. Lett.* **68** 906–908
[6] Li R, Wang Z, Xu B, Jin P, Guo X and Chen M 2006 *Appl. Phys. A* **86** 19–22
[7] Sun X, Rickard W D A, Ironside C N, Kostakis I, Missous M, Powell D, Anjomshoaa A and Meredith W 2021 *Semiconductor Science and Technology* **36** 065015
[8] Todt R, Dovidenko K, Katsnelson A, Tokranov V, Yakimov M and Oktyabrsky S 2001 *MRS Proc.* **692** H9.44.1
[9] Roy S, Maikap S, Sreekanth G, Dutta M, Jana D, Chen Y and Yang J 2015 *J. Alloys Compd.* **637** 517–523
[10] Almuneau G, Bossuyt R, Collière P, Bouscayrol L, Condé M, Suarez I, Bardinal V and Fontaine C 2008 *Semicond. Sci. Technol.* **23** 105021
[11] Verbeeck J and Van Aert S 2004 *Ultramicroscopy* **101** 207–224
[12] Thomas P and Twesten R 2012 *Microsc. Microanal.* **18** 968–969
[13] Egerton R 2011 *Physics of Electron Scattering* (Boston, MA: Springer US) pp 111–229
[14] Rez P 1982 *Ultramicroscopy* **9** 283–288
[15] French R H, Müllejans H and Jones D J 1998 *J. Am. Ceram. Soc.* **81** 2549–2557
[16] Cai W, Li H and Zang Z 2021 *IEEE Electron Device Letters* **42** 525–528 ISSN 1558-0563